Article:
Khosravi, Milad, Butler, Philip, Ahmadi, Hamed orcid.org/0000-0001-5508-8757 et al. (2 more authors) (2025) Advanced ejector design for hydrogen fuel cells using computational simulations and genetic algorithms. International Journal of Hydrogen Energy. 151396. ISSN: 0360-3199

https://doi.org/10.1016/j.ijhydene.2025.151396

International Journal of Hydrogen Energy

Advanced Ejector Design for Hydrogen Fuel Cells Using Computational Simulations and Genetic Algorithms

--Manuscript Draft--

Manuscript Number:	
Article Type:	Full Length Article
Section/Category:	Fuel Cells & Applications
Keywords:	Proton Exchange Membrane Fuel Cells, Hydrogen Recirculation Systems, Ejector Optimization, Computational Fluid Dynamics, Genetic Algorithm.
Corresponding Author:	Elham Hosseinzadeh, PhD University of York York, Yorkshire UNITED KINGDOM
First Author:	Milad Khosravi
Order of Authors:	Milad Khosravi
	Philip Butler
	Hamed Ahmadi
	Andy Tyrrell
	Elham Hosseinzadeh, PhD
Abstract:	Hydrogen recirculation is a key component in Proton Exchange Membrane Fuel Cell (PEMFC) systems, essential for minimizing fuel loss, enhancing efficiency, and supporting water management. This study investigates a passive recirculation strategy using an ejector, an energy-efficient device with no moving parts, making it suitable for applications where simplicity, reliability, and weight are critical, such as in automotive and aerospace sectors. A hybrid computational framework is developed by integrating high-fidelity Computational Fluid Dynamics (CFD) simulations with a Genetic Algorithm (GA) to optimize key ejector parameters, including nozzle radius, exit position, mixing chamber length, and diffuser radius. Optimization is performed directly on full CFD simulations using a high-performance computing cluster, avoiding surrogate models and ensuring accuracy. The model is validated against experimental and theoretical data from the literature. Optimization aims to maximize suction capacity based on a commercial 110-cell PEMFC stack rated at 20.4 kW, operating between 0 and 180 A. The resulting design achieves stable performance from 48 A upwards, significantly broadening the operational range compared to prior ejector configurations. In addition to providing a technical solution for fuel cell gas management, this study establishes a transferable optimization methodology that can support ejector integration in other clean energy systems.

Cover Letter

Elham Hosseinzadeh
Lecturer in the School of PET
(Physics, Engineering and Technology)

M: +44 (0)7446455966
E: eli.hosseinzadeh@york.ac.uk

15th July 2025
The Editors-in-Chief
Journal of Hydrogen Energy

Dear Editor,

Enclosed please find our manuscript entitled *"Advanced Ejector Design for Hydrogen Fuel Cells Using Computational Simulations and Genetic Algorithms"*, authored by Milad Khosravi, Philip Butler, Hamed Ahmadi, Andy Tyrrell, and Elham Hosseinzadeh. We are submitting this manuscript for consideration for publication in the *Journal of Hydrogen Energy*. We confirm that this submission is original, has not been previously submitted to *Hydrogen Energy* (in whole or in part), and is not under consideration for publication elsewhere. The manuscript has been approved by all authors and the relevant host institutions.

This study presents a computationally efficient approach for optimizing ejector designs in hydrogen fuel cell systems, by integrating numerical modelling, genetic algorithms, and experimental validation. Our proposed design framework achieves up to a 20% improvement in hydrogen entrainment, which directly contributes to enhancing the energy efficiency and overall performance of low-temperature fuel cells.
The key novelties of our work include:

1. Establishment of a modular, parameter-driven ejector modelling framework enabling geometry-independent analysis and design
2. A novel integration of a Genetic Algorithm-based optimisation framework into a modular ejector model, enabling rapid, application-agnostic design exploration.

Thank you for considering our manuscript for publication. Please do not hesitate to contact me if further information is required during the review process.

Yours Sincerely,
Elham Hosseinzadeh

University of York
York YO10 5DD
york.ac.uk

Highlights:

- Direct CFD-GA integration for innovative ejector design in hydrogen fuel cells
- Developed ejector achieving robust performance at medium-high currents
- Genetic algorithm navigates complex multi-parameter ejector optimization space
- Computational framework improves hydrogen recirculation system efficiency
- Novel methodology enhances clean energy technology perform

Advanced Ejector Design for Hydrogen Fuel Cells Using Computational Simulations and Genetic Algorithms

Milad Khosravi [a], Philip Butler [b], Hamed Ahmadi [a], Andy Tyrrell [a], Elham Hosseinzadeh [a*]

[a] School of Physics, Engineering and Technology, University of York, York, YO10 5DD, UK

[b] Rolls-Royce plc, PO Box 31, Moor Lane, Derby DE24 8BJ

* Correspondence: eli.hosseinzadeh@york.ac.uk

Abstract

Hydrogen recirculation is a key component in Proton Exchange Membrane Fuel Cell (PEMFC) systems, essential for minimizing fuel loss, enhancing efficiency, and supporting water management. This study investigates a passive recirculation strategy using an ejector, an energy-efficient device with no moving parts, making it suitable for applications where simplicity, reliability, and weight are critical, such as in automotive and aerospace sectors. A hybrid computational framework is developed by integrating high-fidelity Computational Fluid Dynamics (CFD) simulations with a Genetic Algorithm (GA) to optimize key ejector parameters, including nozzle radius, exit position, mixing chamber length, and diffuser radius. Optimization is performed directly on full CFD simulations using a high-performance computing cluster, avoiding surrogate models and ensuring accuracy. The model is validated against experimental and theoretical data from the literature. Optimization aims to maximize suction capacity based on a commercial 110-cell PEMFC stack rated at 20.4 kW, operating between 0 and 180 A. The resulting design achieves stable performance from 48 A upwards, significantly broadening the operational range compared to prior ejector configurations. In addition to providing a technical solution for fuel cell gas management, this study establishes a transferable optimization methodology that can support ejector integration in other clean energy systems.

Keywords: Proton Exchange Membrane Fuel Cells, Hydrogen Recirculation Systems, Ejector Optimization, Computational Fluid Dynamics, Genetic Algorithm.

1 Introduction

The growing global concerns regarding environmental challenges and the necessity to reduce greenhouse gas emissions have led to significant developments in clean energy production technologies. In this regard, Proton Exchange Membrane Fuel Cells (PEMFC) have attracted particular attention due

to their advantages, including high electrochemical efficiency, silent operation, low operating temperature, and rapid load response capability [1].

To ensure stable operation of PEMFC systems, the input fuel typically exceeds the stoichiometric amount required for electrochemical reactions, necessitating fuel recycling. The hydrogen recirculation system (HRS) plays a vital role in returning unreacted hydrogen and water vapor to the fuel cell input while maintaining optimal humidity levels and preventing anode flooding. This process also enables safe management of exhaust gases, as direct hydrogen discharge could pose safety and environmental hazards [2].

In hydrogen recirculation systems, pumps and ejectors are the most common mechanisms, with ejectors gaining particular attention due to their simple structure which comprises of four main parts: primary nozzle, suction chamber, mixing chamber, and diffuser [1,3]. Ejectors, operating on Bernoulli's principle and momentum transfer [4], offer significant advantages over pumps. Their lack of moving parts translates to increased durability, reduced maintenance costs, and quiet operation [3].

Ejectors must be designed to ensure adequate suction capability under diverse operating conditions, posing significant challenges in their optimal design. Innovative solutions, such as variable geometry ejectors [5] and multi-nozzle systems [6], have been proposed to address these issues. However, these approaches introduce complexities, including higher structural intricacy, elevated production costs, and advanced control requirements.

Research has shown that ejector performance is strongly influenced by geometric parameters (e.g., primary nozzle area ratio, nozzle exit position, mixing chamber length, and diffuser angle) and operating conditions [7-10]. While experimental methods have been employed to study these factors [11], they are constrained by high costs, time requirements, and limited test scope. Alternatively, CFD has emerged as a robust method for modelling and optimizing ejector performance, offering high accuracy, efficient computational speed, multi-parameter analysis, and cost-effectiveness. He et al. [12] investigated the influence of primary flow nozzle exit area, secondary flow convergence angle, and nozzle exit position (NXP) on CO2 ejector performance. Liu et al. [13] conducted CFD simulations on transcritical CO2 ejectors in supermarket refrigeration. Li et al. [14] analyzed the impact of mixing chamber dimensions and diffuser angle on rectangular CO2 ejector entrainment ratio using a non-equilibrium CFD model. Liu et al. [15] examined the impact of ejector geometry and operating conditions in transcritical CO2 air conditioning systems. Wu et al. [16] performed multi-parameter analysis using CFD and orthogonal experiments, identifying nozzle exit diameter as the most significant factor. Le Tri et al. [17] focused on optimizing ejector parameters for anode recirculation in high-performance PEMFC fuel cells. Yan et al. [18] investigated the influence of six crucial geometric parameters on ejector performance. Kim et al. [19] proposed a variable multiple ejector system for a minibus fuel cell system. Brunner et al. [20] designed an electronically controlled variable flow ejector

for the Ballard Mark 9 stack. Pei et al. [21] conducted numerical studies on wide-range operating ejectors based on anode pressure drop characteristics in PEMFC systems. Kandakure et al. [22] performed comprehensive CFD studies on ejector hydrodynamics. Zhu et al. [23] investigated the effects of NXP and mixing section convergence angle on ejector performance.

Previous research on ejector performance optimization has primarily relied on a case-by-case approach, which is limited by the vast design space and complex interactions between ejector components. This makes achieving optimal geometry through traditional parametric studies time-consuming and inefficient. To address these limitations, researchers have turned to artificial intelligence (AI) methods [24-26]. AI excels in optimizing ejector geometry by effectively exploring the multi-dimensional design space, modelling complex nonlinearities, avoiding local optima, and significantly reducing the number of required evaluations. Liu et al. [27] presented a multi-objective optimization framework for CO2 ejector systems by combining Artificial Neural Network (ANN) and Non-dominated Sorting Genetic Algorithm II (NSGA-II). Pang et al. [28] introduced a comprehensive framework for performance prediction and geometry optimization of ejectors in PEMFC systems, combining CFD simulation, backpropagation neural network (BPNN), and genetic algorithms. Arabbeiki et al. [1] focused on optimizing hydrogen recirculation systems in PEMFC fuel cells using CFD simulation. Maghsoodi et al. [29] investigated the impact of four key geometric parameters on ejector performance and developed an optimized design using CFD simulation, ANN, and GA. Liu et al. [30] presented a framework for optimizing two-phase CO2 ejector performance by combining CFD, ANN, and GA. Palacz et al. [31] developed software enabling integration with commercial CFD solvers using two intelligent optimization algorithms (genetic and evolutionary algorithms). Palacz et al. [32] employed genetic algorithm and homogeneous equilibrium model (HEM) to optimize various ejector parameters. Carrillo et al. [33] utilized multi-objective evolutionary algorithm and CFD-based surrogate model for optimizing geometric structures of air and CO2 ejectors. Ringstad et al. [34] employed CFD data to train a Gaussian Process Regression (GPR) machine learning model and used the combination of machine learning model and gradient descent method to identify optimal CO2 ejector geometric structures. Li et al. [35] optimized geometric structures of a rectangular CO2 ejector using CFD simulation, response surface methodology (RSM), and genetic algorithm. Song et al. [36] proposed an RSM-based multi-objective genetic algorithm for optimizing ejector performance in SOFC systems. Srisha Rao and Jagadeesh et al. [37] employed vector-evaluated particle swarm multi-objective optimization algorithm to optimize ejector design. Gil and Kasperski [38] evaluated ejector cycle performance using ethers and fluorinated ethers as refrigerants and focused on their performance optimization.

This study introduces a novel optimization framework for hydrogen ejector design in PEM fuel cells, directly coupling high-fidelity CFD simulations in OpenFOAM with a genetic algorithm. In contrast to previous work that relies on surrogate models or simplified geometries, this approach performs full-

order simulations throughout the optimization, accurately capturing complex, compressible flow behaviour. Deployed on a high-performance computing cluster, the framework enables multi-parameter optimization of ejector geometry and delivers a single design with stable suction performance across a wide fuel cell operating range. Beyond PEMFC applications, the methodology is transferable to other systems requiring passive recirculation or gas entrainment, offering a generalizable tool for advanced ejector design across various clean energy technologies.

The rest of the paper is structured as follows: the introduction outlines the research motivation and background. The methodology begins by describing the studied fuel cell system and its model, followed by an explanation of the ejector's numerical model and the optimization process. The results section discusses the findings and their validation, and the conclusion highlights the contributions and future directions of the study.

2 Fuel Cell System Description

This study utilizes Ballard's fuel cell stack, consisting of 110 cells, with each cell having an active area (A) of 285.88 cm^2. The system configuration and fuel cell stack are similar to those presented by Rabbani and Rokni [39], Liso et al. [40], Hosseinzadeh and Rokni [41], and Hosseinzadeh et al. [5]. However, the goal is to design an ejector that can maximize the operating range of the anode recirculation system, effectively replacing the electric pump across varying operating conditions, from low to high current (I). Figure 1 presents the schematic of the system and its components. The operating temperature (T_{ope}) ranges from 60 to 70°C. The maximum output power (P_{total}) of this system is approximately 20.4 kilowatts. The inlet gas temperature is around 60°C. The fuel inlet pressure is adjusted by a pressure regulator according to operating conditions. The stoichiometry of fuel (An_{Sto}) and air (Cat_{Sto}) varies depending on the current flow, with values of 1.6 and 1.8 at higher power levels, respectively. This fuel cell employs a water exchange method between the anode and cathode, eliminating the need for additional humidification on the anode side. The relative humidity at the cathode inlet is approximately 95 percent. A zero-dimensional analytical model for simulating the performance of PEMFC has been implemented using Python programming language. The developed model estimates cell voltage based on activation, ohmic, and concentration potentials, which can be used to generate polarization curves and estimate cell performance under various conditions [42, 43]. Additionally, this model simulates water transport through the membrane, considering mechanisms such as osmosis, diffusion, and hydraulic permeation [42, 43]. This is a complex and important phenomenon that have a big impact on the anode and cathode water content, and consequently on the ejector design.

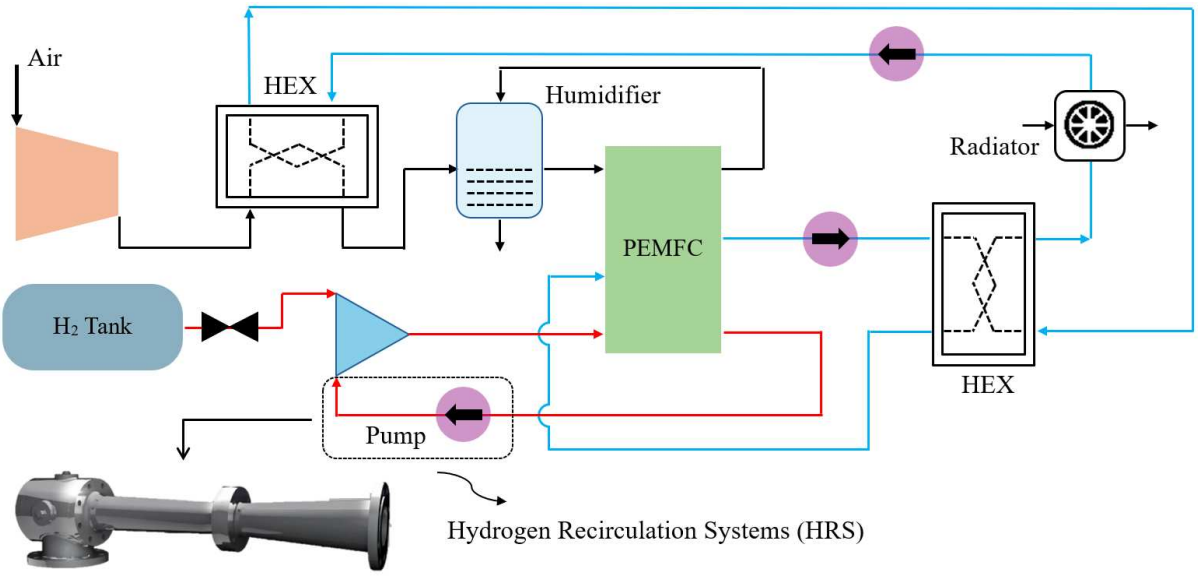

Figure 1. The schematic of the Ballard's fuel cell system configuration and its components (Air and hydrogen tank, Humidifier, Pump, Radiator, and Heat Exchanger).

2.1 Operating conditions of the system

In this research, the studied ejector is designed to supply the hydrogen required for the fuel cell, in accordance with the operational conditions proposed by Ballard [39-41, 5]. The operational conditions for the Ballard stack are presented in Table 1, where T1 to T5 represent different operating conditions. The final column of Table 1 shows the entrainment ratio, defined as the ratio of the secondary flow's mass flow rate to the primary flow's mass flow rate.

Table 1. Operating conditions for fuel cell stack recommended by manufacturer (Ballard).

Case	I [A]	A [cm^2]	P_{total} [W]	An_{Sto} [-]	Cat_{Sto} [-]	T_{ope} [K]	P_{an} [bar]	P_{cat} [bar]	Entrainment ratio [-]
T1	15	285.8	1414	6.3	5.1	334.15	1.15	1.08	16.34
T2	30	285.8	2723	3.4	2.4	336.15	1.16	1.10	8.09
T3	60	285.8	5201	2.2	1.8	339.15	1.31	1.17	4.25
T4	120	285.8	9794	1.9	1.8	340.15	1.57	1.35	2.83
T5	180	285.8	14157	1.6	1.8	340.65	1.92	1.58	1.72

The primary objective of this study is to enhance the entrainment ratio within the system by maximizing the secondary flow rate. This is accomplished through the optimal design of an ejector that maximizes the operational range of the fuel cell across varying conditions, from low to high current.

3 Computational Model and Numerical Framework of Ejector:

A schematic of the ejector is presented in Figure 2. The primary flow comprises pure pressurized hydrogen at 25°C, while the secondary flow consists of unreacted hydrogen from the fuel cell mixed

with water vapor. The operating temperature of the secondary flow aligns with the fuel cell's operating conditions.

3.1 Computational Domain and Boundary Conditions

A 2D axisymmetric model has been used to model the ejector, where the x-axis represents the axis of symmetry of the model. The geometric configuration depicted in Figure 2 is characterized by the following parameters: primary nozzle throat radius (R_{th}); mixing chamber radius (R_m); diffuser radius (R_d); nozzle exit position (L_s); mixing chamber length (L_m); and diffuser length (L_d).

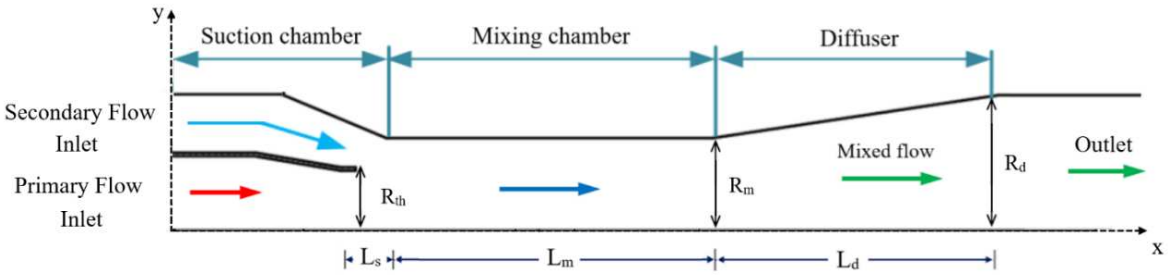

Figure 2. Schematic of the computational domain geometry, illustrating the arrangement and dimensions of the suction chamber, mixing chamber, and diffuser.

The boundary conditions include constant temperature at the primary and secondary inlets. At the primary inlet, a mass flow rate boundary condition is imposed for velocity, and a zero-gradient boundary condition is applied for pressure. The boundary condition for velocity on the walls is a no-slip condition. At the walls, the wall functions are used to estimate the turbulence parameters k, ε and μ_t [44]. For the pressure at the outlet and secondary inlet, a static pressure boundary condition is used. The other boundary conditions are of type zero gradient.

3.2 Governing equations

The three-dimensional Unsteady Reynolds-averaged Navier–Stokes (URANS) equations are used as follows:

Continuity equation:

$$\frac{\partial \rho}{\partial t} + \frac{\partial \rho \bar{u}_i}{\partial x_i} = 0.0 \qquad i = 1, 2, 3, \tag{1}$$

Momentum equation:

$$\frac{\partial \rho \bar{u}_i}{\partial t} + \frac{\partial \left(\rho \bar{u}_i \bar{u}_j\right)}{\partial x_j} - \mu \Delta^2 \bar{u}_i + \frac{\partial \left(\overline{\acute{u}_i \acute{u}_j}\right)}{\partial x_j} = -\frac{\partial \bar{P}}{\partial x_i} + \rho g_i, \tag{2}$$

Energy equation:

$$\frac{\partial \rho \bar{T}}{\partial t} + \frac{\partial \left(\rho \bar{u}_j \bar{T}\right)}{\partial x_i} = \frac{\partial}{\partial x_j}\left(\lambda \frac{\partial \bar{T}}{\partial x_j}\right) - \frac{\partial \left(\overline{\acute{u}_j \acute{T}}\right)}{\partial x_i} - \left(\frac{\partial (P \bar{u}_i)}{\partial x_i} + \frac{\partial (\rho K)}{\partial t} + \frac{\partial (\rho K \bar{u}_i)}{\partial x_i}\right)\left(\frac{\alpha_1}{C_{v1}} + \frac{\alpha_2}{C_{v2}}\right) \tag{3}$$

where $\bar{u}_i$, P, T, t and μ represent the time-averaged velocity components, pressure, temperature, time and molecular viscosity, respectively. λ = μ/Pr is the molecular heat transfer coefficient, Pr is the Prandtl number. With i = 1, 2, 3 indicates the velocity components in the x, y and z directions, respectively. α_1 and α_2 are the phase volume fractions. C_{v1} and C_{v2} are the specific heat capacities at constant volume for the respective phases.

ρ is the density of the fluid which is determined by the state equation. Here, the perfect gas law is used to calculate the density:

$$\rho = \frac{PM}{RT}, \tag{4}$$

where R is the gas constant and M is the molar mass of the gas.

The effect of turbulence in URANS equations is calculated through the Reynolds stress tensor term ($\overline{\acute{u}_\iota \acute{u}_\jmath}$) and the turbulent heat flux term ($\overline{\acute{u}_\jmath \acute{T}}$). Using the Linear Eddy Viscosity (LEV) approach, these two parameters are calculated as follows:

$$-\overline{\acute{u}_\iota \acute{u}_\jmath} = \mu_t \left(\frac{\partial \rho \bar{u}_i}{\partial x_j} + \frac{\partial \rho \bar{u}_j}{\partial x_i} \right) - \frac{2}{3} \delta_{ij} k, \tag{5}$$

$$-\overline{\acute{u}_\jmath \acute{T}} = \frac{\mu_t}{Pr_t} \frac{\partial \bar{T}}{\partial x_j} \qquad i = 1, 2, 3, \tag{6}$$

Where δ_{ij} is the Kronecker delta ($\delta_{ij} = (0 \ \ if \ i \neq j; \ \ 1 \ \ if \ i = j)$), Pr_t is the turbulent Prandtl number. μ_t is the turbulent viscosity which is calculated by the turbulence model. In this study, the k-ε RNG turbulence model is used. In this turbulence model, μ_t is calculated by solving the transport equations of turbulent kinetic energy (k) and its rate of dissipation (ε) as shown below:

$$\frac{\partial (\rho k)}{\partial t} + \frac{\partial (\rho k \bar{u}_i)}{\partial x_j} = \frac{\partial}{\partial x_j} \left[\left(\mu + \frac{\mu_t}{\sigma_k} \right) \frac{\partial k}{\partial x_j} \right] + \mu_t S^2 - \rho \varepsilon, \tag{7}$$

$$\frac{\partial (\rho \varepsilon)}{\partial t} + \frac{\partial (\rho \epsilon \bar{u}_i)}{\partial x_j} = \frac{\partial}{\partial x_j} \left[\left(\mu + \frac{\mu_t}{\sigma_k} \right) \frac{\partial \varepsilon}{\partial x_j} \right] + C_{\varepsilon 1} \frac{\varepsilon}{k} \mu_t S^2 - C'_{\varepsilon 2} \rho \frac{\varepsilon^2}{k}, \tag{8}$$

$$\mu_t = C_\mu \frac{k^2}{\varepsilon}, \tag{9}$$

where,

$$S = \sqrt{2 S_{ij} S_{ij}} \quad ; \quad S_{ij} = \frac{1}{2} \left(\frac{\overline{\partial u_i}}{\partial x_j} + \frac{\overline{\partial u_j}}{\partial x_i} \right); \ C'_{\varepsilon 2} = 1.68 + \frac{0.085 \lambda^3 (1 - \lambda / 4.38)}{1 + 0.012 \lambda^3}; \quad \lambda = \frac{k}{\varepsilon} S. \tag{10}$$

σ_k and σ_ε are the turbulent Prandtl numbers for the turbulent kinetic energy transport equation and its dissipation rate equation and are equal to 1.0 and 1.3, respectively. $c_{\varepsilon 1}$ and $c_{\varepsilon 2}$ are model constants and are equal to 1.44 and 1.92, respectively. The other constants are as follows:

$$C_\mu = 0.09 \ \ ; \ \ \sigma_k = 0.72 \ \ ; \ \ \sigma_\varepsilon = 0.72.$$

3.3 Numerical method

The open-source computational fluid dynamics code OpenFOAM version 9 based on the finite volume method has been used for the simulations. The governing equations are solved by the standard *compressibleInterFoam* solver, which is a solver for two compressible, non-isothermal and immiscible fluids that utilizes a volume of fluid (VOF) phase-fraction based interface capturing approach.

The solver uses the PIMPLE (merged PISO-SIMPLE) algorithm for pressure-momentum coupling. This algorithm leverages the strengths of both PISO and SIMPLE methods for pressure-velocity coupling, ensuring robustness in handling transient flows with large time steps. The time derivatives are discretized by the implicit first order accurate Euler scheme. The Gauss linear method is adopted for the gradient interpolation. The Gauss limited linear schemes have been used to discretize for all the convective terms. The Laplacian terms are discretized using limited Gauss linear corrected schemes.

The iterative solver for symmetric and asymmetric matrices which uses a *symGaussSeidel* smoother to converge the solution is applied for the pressure and phase volume fractions field with a tolerance of $10e^{-6}$. While the stabilized preconditioned (bi-) conjugate gradient method, for both symmetric and asymmetric matrices, with diagonal incomplete LU (DILU) preconditioner is applied for U, T, k, and ε with a tolerance of $10e^{-6}$. Preconditioned conjugate gradient (PCG) with Simplified Diagonal-based Incomplete Cholesky (DIC) preconditioner is used to solve the density field with a tolerance of $10e^{-5}$ at each time step.

All simulations were conducted on a high-performance computing system (the Viking cluster). The cluster comprises 134 standard compute nodes, each equipped with two AMD EPYC 3 7643 processors (48 cores each), totalling 12,864 CPU cores. Each standard compute node features 512 GB of memory. For each simulation case, parallel computations were performed exclusively on the cluster's CPU resources, leveraging the multi-core architecture of the AMD EPYC processors to accelerate the simulation process.

4 Optimization Process

4.1 Genetic Algorithms

In this study, a Genetic Algorithm (GA) was employed to optimize the geometry of the ejector. The GA is an advanced optimization technique inspired by the principles of natural selection and genetics [45]. GAs have been widely applied across diverse fields such as engineering, computer science, economics, and biology. They are particularly noted for their ability to explore large and intricate search spaces, making them invaluable for solving problems where conventional optimization methods are inadequate [46]. The flowchart illustrating the implementation of the genetic algorithm in this research is presented in Figure 3.

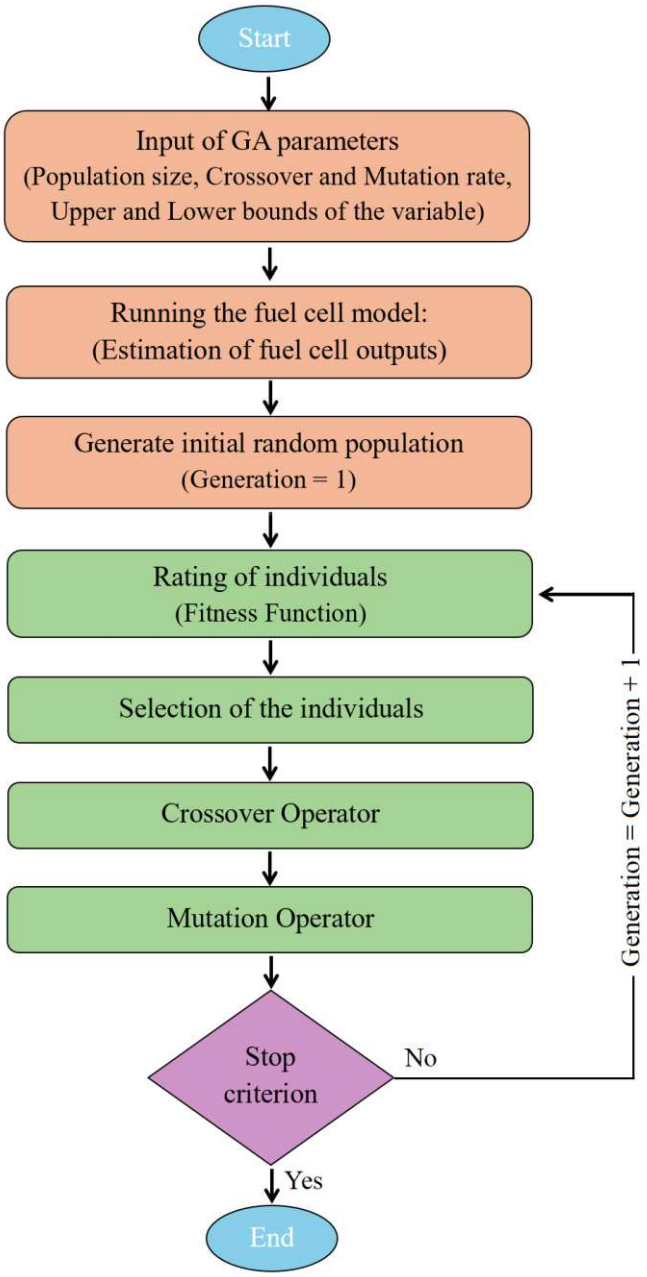

Figure 3. Genetic algorithm flowchart.

In a genetic algorithm, each candidate solution is represented as a chromosome (or individual), serving as the foundation for the optimization process. The initial population was randomly generated within the upper and lower bounds of the design variables, subject to the constraints of the problem. These constraints are detailed in the following section. Subsequently, the selected variables are evaluated using the fitness function, which quantifies the quality of each solution. The details of this evaluation process are elaborated in the following section.

The quality of each individual is assessed, which quantifies its suitability as a solution to the problem. Individuals with higher fitness scores are preferentially selected for reproduction through various selection mechanisms. In this study, roulette wheel selection was employed as the method for parent

selection. This technique assigns selection probabilities to individuals proportionate to their fitness levels, with individuals of higher fitness occupying larger segments of the roulette wheel, thereby increasing their chances of being selected.

The selected parents underwent recombination using the continuous crossover method to generate offspring. In this approach, each gene in the offspring was calculated as a linear combination of the corresponding gene values from the parents, enabling effective exploration of the search space and increasing the likelihood of discovering optimal solutions (Figure 4a). To maintain genetic diversity and prevent premature convergence, a continuous mutation technique was employed. This method introduces a small random variation for a random gene, preserving population diversity and reducing the risk of the algorithm becoming trapped in local optima (Figure 4b). The range of variation for the selected variable is defined as ±C% of its upper (up) and lower (lb) bounds. Preliminary experiments showed that a value of C=10% yielded a good trade-off between diversity and convergence speed in this specific problem.

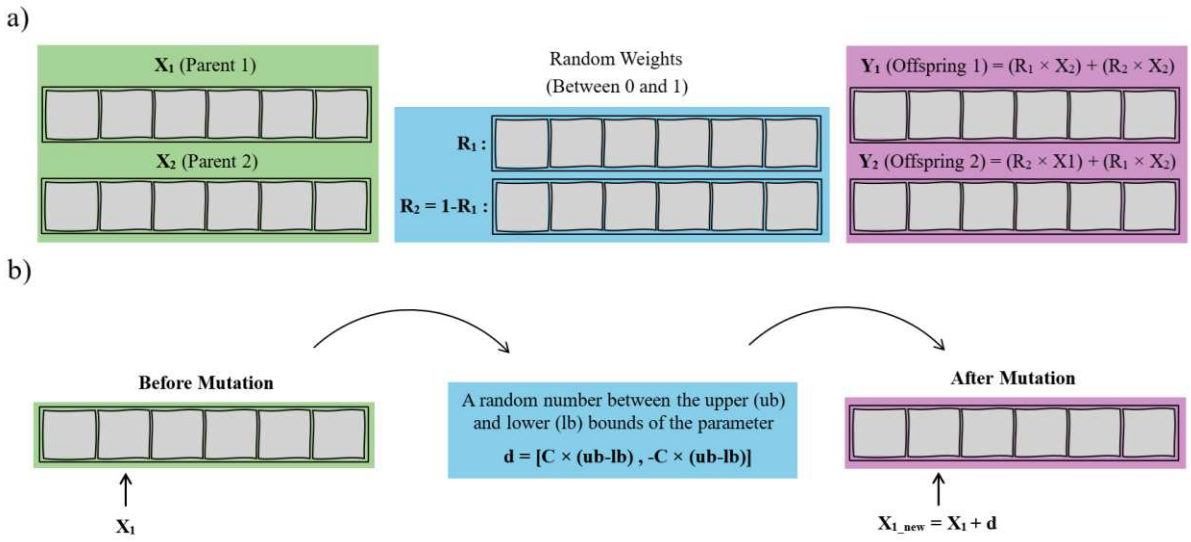

Figure 4. Operations of (a) continuous crossover and (b) continuous mutation from parent selection to offspring generation.

This iterative process—comprising evaluation, selection, crossover, and mutation—continues until a specified termination criterion is satisfied. The stopping criterion for the genetic algorithm was defined based on two conditions: the maximum number of objective function evaluations or the convergence trend in the objective function values. The algorithm continued its execution until either the maximum number of evaluations was reached, or no significant improvement was observed in the best solution or the average fitness of the population. This dual-criterion approach ensured that the algorithm converged to a satisfactory solution while minimizing computational time and avoiding unnecessary exploration.

4.2 Fitness Function

The fitness function comprises three primary components, as illustrated in Figure 5. The process begins with geometry design and meshing, utilizing the geometric parameters defined during the optimization procedure. Subsequently, initial conditions and boundary conditions are established based on the problem specifications in the numerical model. Finally, the numerical model of the ejector, implemented using the open-source OpenFOAM framework, performs an accurate simulation of the fluid flow. The output results, including the suction value at the secondary flow location, are then transmitted to the optimization algorithm for evaluation. To facilitate synchronization between the CFD model and the optimization algorithm, a custom code was developed in the Python programming environment, ensuring seamless integration of these components throughout the optimization process.

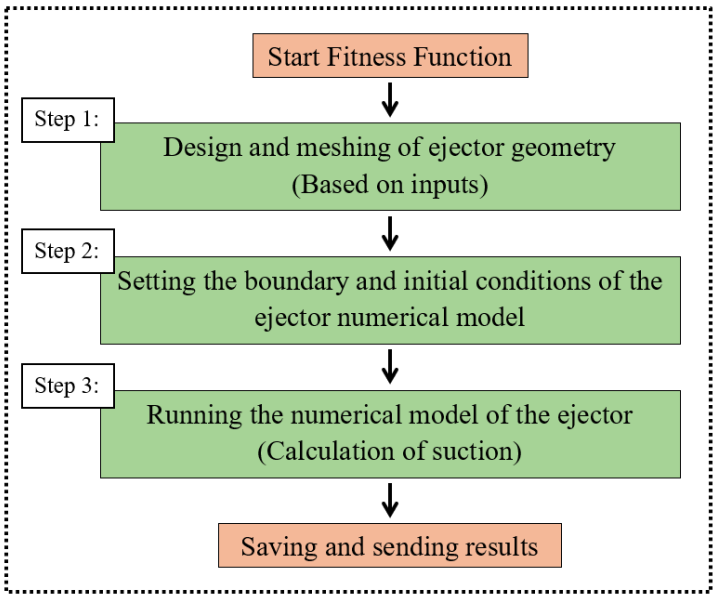

Figure 5. Flowchart of the fitness function for use in the genetic algorithm.

4.3 Defining the Optimization Problem

The optimization objective focuses on maximizing the ejector's suction capacity across a broad current range through optimal geometric configuration. The objective function F(X) is mathematically expressed as:

$$\max F(X) = \dot{m}_s, \tag{11}$$

where $X = [R_{th}, R_m, R_d, L_s, L_m, L_d]$ represents the design variables shown in Figure 2.

Success criteria involve comparing the genetic algorithm-derived optimal solution's suction flow rate against target values specified in Table 1, with achievement or exceedance indicating sufficient ejector capacity for fuel cell gas recirculation.

In addition to the ejector geometric parameters determined in the optimization process, there is a need to precisely define the operating conditions for both the ejector and fuel cell systems. The operating conditions of the ejector include the pressure and temperature of the secondary flow, the mass flow rate

of the primary flow, the outlet pressure, and the properties of the working fluid, which are consistent with the operating conditions of the fuel cell. The fuel cell model parameters include operating temperatures, pressures, Relative Humidity (RH), and stoichiometric hydrogen ratio, which determine the water vapor and excess hydrogen output quantities specific to each case study.

In this study, considering the existing manufacturing constraints of the ejector and the operational conditions outlined in Table 1, the minimum primary nozzle throat radius (R_{min}) was calculated to be 0.2 mm. Given the available computational resources, the upper bound of R_{th} was set to $3.5R_{min}$. Furthermore, the values for R_m and R_d were examined, ranging from 2.5 to 15 times and 2.5 to 35 times the R_{min}, respectively. A review of the literature indicated that various optimal dimensional ratios, expressed as length-to-radius ratios, have been proposed for different sections of the ejector. To thoroughly encompass these proposals, this research explored a broad range of these ratios. The values of L_m and L_d were investigated from 3 to 60 times and 5 to 18 times their respective radii, respectively. Additionally, the L_s was set to a maximum of 35 times the R_{min}. These values were established as the upper and lower bounds for the design variables.

5 Results and discussion

5.1 Validation of the fuel cell

The analytical fuel cell model was validated with the data presented in Table 1, obtained from the Ballard Power Systems fuel cell stack. The comparison between experimental data (symbols) and analytical results (solid line) in Figure 6 shows excellent agreement, confirming the model's accuracy.

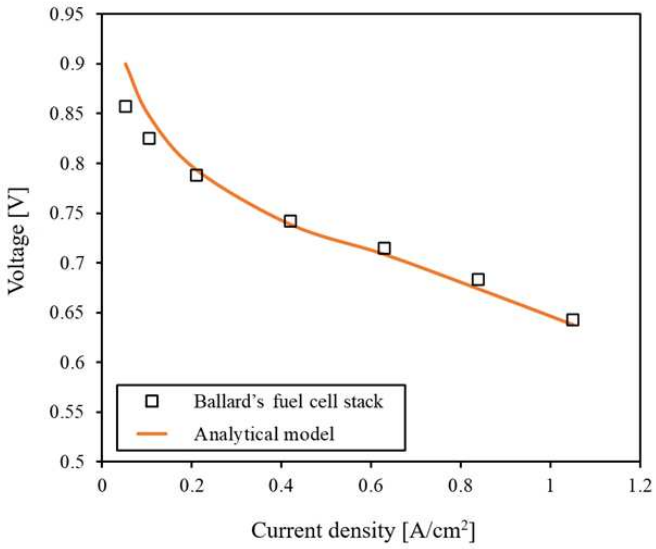

Figure 6. Comparison of polarization curves for different fuel cell temperatures. Symbols represent Ballard's fuel cell stack data, while the solid line depicts the analytical model results.

5.2 Validation of the Ejector

To validate the CFD numerical model, theoretical data from Marsano et al. [47] was used, in this work they designed an anode-based ejector recirculation system for hybrid solid oxide fuel cell (SOFC) applications. The ejector geometry was optimized based on specified operating conditions including primary mass flow rate, secondary flow pressures, temperatures, and gas compositions, as detailed in Table 2. Under these conditions, their design achieved a secondary mass flow rate of 0.0677 kg/s and an entrainment ratio of 7.20. Here, given that the pressure value at the primary flow inlet is specified, a total pressure boundary condition is applied to the pressure term, while a zero-gradient boundary condition is applied to the velocity term. Subsequently, the mass flow rates at both the primary and secondary flow locations are analysed for validation purposes.

Table 2. Design point values of ejector

Parameter	Marsano et al. [47]	Present study (CFD)
Primary flow composition (molar, %)	CH_4 (100)	CH_4 (100)
Secondary flow composition (molar, %)	H_2 (0.39); CO (4.19); H_2O; (43.96); CO_2 (51.46)	Average value of compositions
Primary mass flow rate (kg s-1)	0.0094	0.0092
Secondary mass flow rate (kg s-1)	0.0677	0.0676
Primary flow pressure (bar)	10.06	10.06
Secondary flow pressure (bar)	3.8	3.8
Outlet pressure (bar)	3.6	3.6
Primary flow Temperature (K)	673	673
Secondary flow Temperature (K)	1280	1280

A structured mesh with cubic elements has been utilized for the grid generation. Following a sensitivity analysis on the mesh, 10 elements were employed in the radial direction for the primary flow region, and 12 cells were used for the secondary flow region. In the longitudinal direction of the channel, a total of 139 cells were implemented. Figure 7 illustrates the results of the mass flow rate of the secondary flow recorded throughout the analysis, compared to the data from Marsano et al. [47]. As observed, the value of the secondary flow was calculated to be approximately 0.0676 kg/s. Due to some fluctuations in the data, an average value was taken within the time interval of 0.04 sec to 0.05 sec. This meshing also led to an estimation of the mass flow rate of about 0.0092 kg/s, which shows a very good agreement with the reported value.

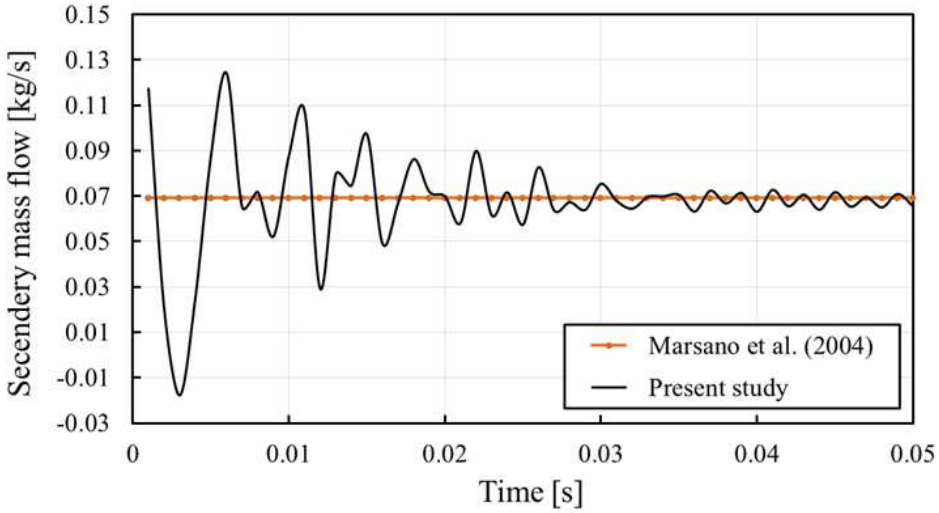

Figure 7. Comparison of Marsano et al. [47] data with results from the present numerical model for mass flow rate at the secondary flow inlet.

5.3 Genetic algorithm

The genetic algorithm implemented in this study utilized an initial population composed of 50 individuals. From this population, 34 offspring were generated through the crossover process, while 16 offspring were produced via mutation. Since the whole process is stochastic, it is essential to run the algorithm multiple times to ensure the results have statistical relevance. To visualize the results and facilitate statistical analysis, box and whisker plots were employed. This type of plot is a useful tool for analyzing the results of genetic algorithms clearly illustrating the stability, dispersion and optimality of the results.

To examine the optimization process in each analysis, Figure 8 presents a sample of the Box Plots for different generations from the analysis for case T3. Analysis of the Box Plot for successive generations of the genetic algorithm shows significant dispersion in the results of the first generation, evident from the large box and long whiskers in the plot. This high diversity in the initial population is desirable from a genetic algorithm perspective as it enables searching through a broader solution space. From the second generation onwards, a gradual and distinct improvement trend can be observed through the decreasing size of boxes (IQR), movement of medians towards better values, and reduction in the number of outliers. This trend indicates the gradual convergence of the population towards optimal solutions. From the eighth generation onwards, changes become minimal, which can be observed from the stability in box sizes, median positions, and significant reduction in outliers. This stability indicates that the algorithm has reached a steady convergence point.

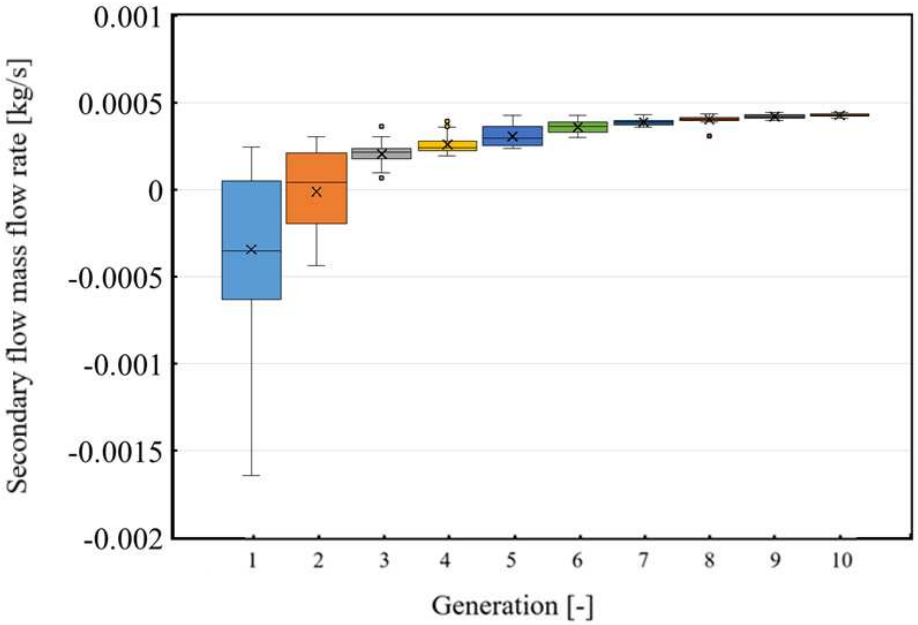

Figure 8. Box Plots displaying the distribution of data for each generation in case T3, illustrating the median, quartiles, and outliers within the dataset.

The appropriate convergence speed, occurring within about eight generations, demonstrates the proper performance of crossover and mutation operators. This also indicates the success of the parent selection strategy and elitism in the algorithm. The gradual reduction in variance, observable through the shrinking boxes, along with continuous improvement in medians, shows that the algorithm has managed to establish an appropriate balance between exploration of the search space and exploitation of good solutions, reaching a stable and acceptable convergence.

In this study, the algorithm was executed 30 times, which allows for a robust assessment of the outcomes and enhances the reliability of the findings. Figure 9 illustrates the distribution of results from 30 optimization runs for cases T3. In the presented graph, points represent the outlier value obtained in a genetic algorithm execution.

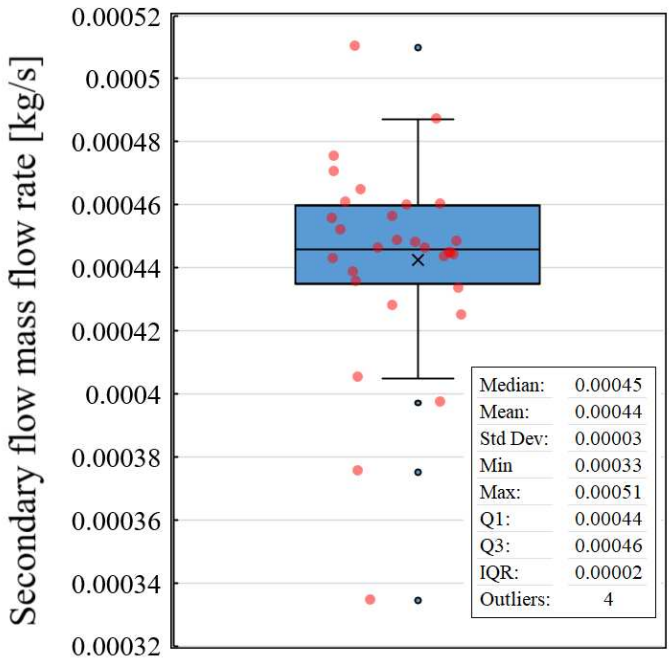

Figure 9. Box and whisker plot showing the results of 30 optimization runs for case T3.

Analysis of the box plot reveals that the GA demonstrated satisfactory performance over 30 executions. The mean objective function value of 0.00044 and median of 0.00045 are relatively close, indicating a symmetric distribution of results. The small standard deviation (0.00003) compared to the mean suggests low data dispersion around the average and highlights the algorithm's stability in producing consistent results. The Interquartile Range (IQR), calculated as the difference between the third quartile (0.00046) and first quartile (0.00044), equals 0.00002. This small range confirms that the central 50% of the data is concentrated in a narrow interval, reinforcing the algorithm's reliability and reproducibility. In this dataset, 4 outliers are observed, including one at the maximum value of 0.00051. The presence of an outlier at the highest observed value is particularly beneficial in optimization problems, as it represents a superior solution achieved in at least one execution. The remaining outliers, which are significantly lower than the interquartile range, can be attributed to the stochastic nature of the genetic algorithm and occasional convergence to suboptimal solutions. However, the low number of such deviations suggests that the algorithm successfully converged to desirable and consistent results in most cases. The concentration of most data points in the upper region of the plot and near the best solution demonstrates that the algorithm frequently identified high-quality solutions. This consistency is a key advantage in optimization, as it reflects the algorithm's strong capability in navigating the search space effectively and avoiding poor local optima. Overall, based on the statistical metrics and result distribution, the designed GA has performed well in terms of stability, reproducibility, and its ability to achieve optimal solutions, with at least one run reaching the highest observed performance.

5.4 Optimized ejector design using CFD and genetic algorithm

In the present study, all the cases of Table 1 were investigated to design an optimal ejector for the fuel cell. The results indicate that it is not possible to achieve a design that has adequate suction capability for the 15 and 30 A cases. Further investigations for the 60, 120 and 180 A cases resulted in a design that has sufficient suction capability according to the values in Table 1 and can effectively remove all excess gases from the fuel cell. However, the optimized geometries for the 120 and 180 A cases lead to the identification of high radii for the nozzle, which reduces the suction capability at lower currents. Hence, the 60 A case was selected for optimization. Table 3 shows the optimal geometric dimensions of the ejector identified by the genetic algorithm for the T3 case. In addition, the final column of Table 3 provides the estimated bubble ratio.

Table 3. Predicted dimensions of the ejector using the genetic algorithm method.

Case	L_s [mm]	L_m [mm]	L_d [mm]	R_{th} [mm]	R_m [mm]	R_d [mm]	Suction [kg/s]	Entrainment ratio [-]
T3	0.28	16.0	45.45	0.23	1.5	5.09	0.0005133	7.45

From a practical perspective, it is essential to select a specific fuel cell that addresses the problem at hand. To achieve this, one design is chosen as the optimal configuration for each scenario, and the suction capabilities of other configurations (as detailed in Table 1) are assessed in relation to the selected design. Figure 10 presents the profiles of secondary flow rates suctioned by the chosen optimal ejector as a function of current. It also illustrates the design points representing the suction requirements necessary for the ejector. Additionally, the figure depicts the three-dimensional geometries of the T3 design. As shown in the figure 10, comparing the T3 design with the design points, which represent target performance values, at low currents (below 48 A), the T3 design exhibits no suction capability, as indicated by the dashed line. However, there is a sharp increase in performance at approximately 45-60 A, where the secondary flow rate rises dramatically to around 0.0005 kg/s. Beyond this point, the T3 design shows a steady, nearly linear increase in secondary flow rate, reaching approximately 0.00065 kg/s at 120 A and ultimately achieving its maximum performance of about 0.00078 kg/s at 180 A, which significantly exceeds the required design points. When comparing these findings with Hosseinzadeh et al. [5], the T3 design shows improvements. While Hosseinzadeh et al. [5] encountered operational constraints below 60 A, with their system being unable to generate suction below 50 A, the T3 design pushes this lower operational limit even further down to 48 A. However, once operational, the T3 design demonstrates superior performance in the high-current range, particularly above 85 A, where it achieves significantly higher secondary flow rates than the previous research. This represents a marked improvement over Hosseinzadeh's configuration, which barely met minimum acceptable performance thresholds at 85 A. Based on the comprehensive performance analysis, Design T5 has been selected as

the final optimized ejector configuration due to its effective suction capabilities across the entire required current range, addressing the limitations observed in previous designs.

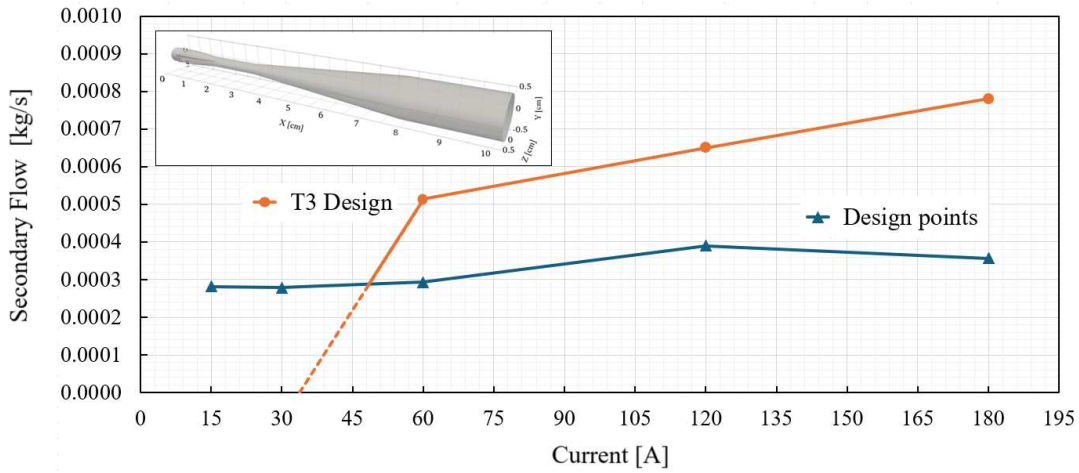

Figure 10. Profiles of the secondary flow rates extracted by the selected optimal ejector, accompanied by the corresponding design points.

Figure 11 illustrates the pressure distribution profile along the x-axis of the ejector for I=60 [A], accompanied by a close-up view of the mixing chamber. The numerical results capture the key flow characteristics, including the sharp drop in pressure near x = 0.02 m, which indicates the presence of a shock due to flow expansion. This phenomenon is followed by a region of relatively stable pressure at approximately 1.1 bar, corresponding to the mixing and stabilization zone of the ejector. Toward the outlet (x>0.033 m), the pressure gradually recovers, reaching around 1.3 bar, representing the recompression zone. The results demonstrate that the numerical model accurately captures the complex pressure variations along the ejector, including the shock phenomenon and pressure recovery. This highlights the model's capability to effectively simulate the ejector's dynamic behaviour and validate its physical performance under the given operating conditions.

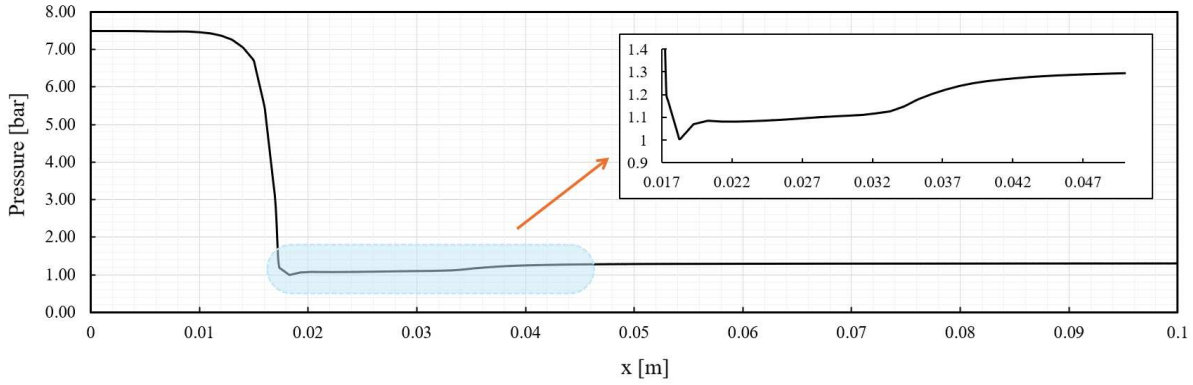

Figure 11. Pressure distribution profile along the x-axis of the ejector for I = 60 A, with a close-up view of the mixing chamber area.

Figure 12 presents the numerical results of velocity and temperature distributions for the ejector with I = 60 A. In the velocity contour (Fig. 12a), following the principles of compressible flow and conservation of mass, the flow behaviour demonstrates a significant acceleration near the throat region (x ≈ 0.02 m), with velocities reaching up to 1919 m/s. According to the ideal gas law, this acceleration corresponds precisely to the pressure drop observed in Figure 11, consistent with Bernoulli's principle in compressible flows. Velocity gradually decreases in the diffuser due to the conservation of mass and momentum within the expanding cross-section. The temperature distribution (Fig. 12b) exhibits a corresponding pattern, following the energy equation and flow relationships, with a minimum temperature of approximately 166 K occurring in the throat region where the flow acceleration is maximum. The temperature gradually increases along the diffuser section as the primary flow mixes with the secondary flow and pressure recovers. These results further validate the numerical model's capability to accurately capture complex flow phenomena, particularly in the shock region where rapid changes in flow properties occur.

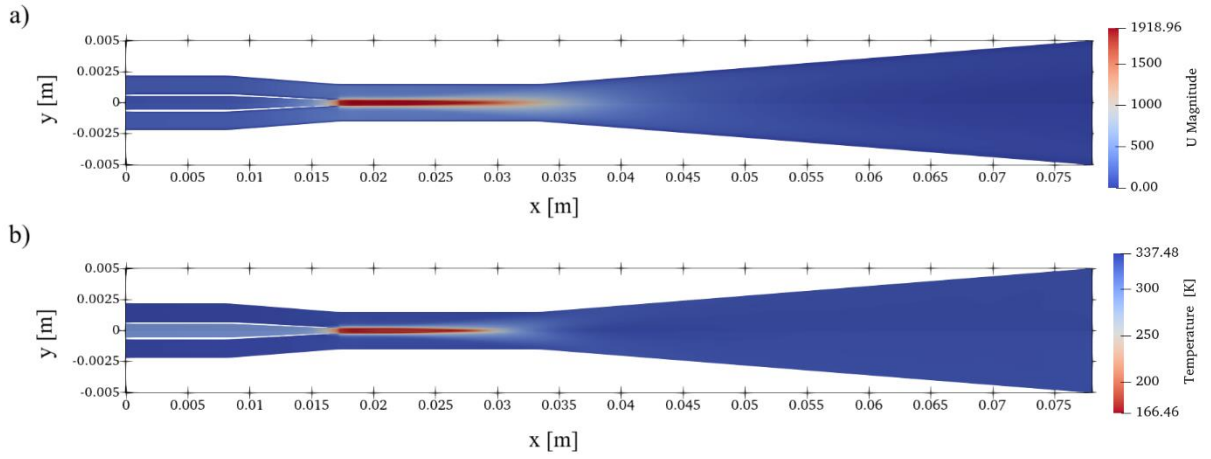

Figure 12. Contour plots of (a) velocity magnitude and (b) temperature distribution within the ejector at an operating current of 60 A.

6 Conclusion

This study developed an advanced optimization framework for the design of ejectors in hydrogen recirculation systems (HRS) for Proton Exchange Membrane Fuel Cells (PEMFC). By directly integrating computational fluid dynamics (CFD) simulations with a genetic algorithm (GA), the framework effectively addressed the limitations of conventional surrogate-based methods. The proposed approach enabled the comprehensive exploration of key geometric parameters, including position and radius of the nozzle, mixing chamber dimensions, and diffuser length. Validation against experimental data confirmed the reliability and accuracy of the proposed CFD model.

Based on a comprehensive performance analysis, Design T3 (60 A) demonstrates significant improvements compared to previous designs, although it cannot cover the entire required current range.

It shows remarkably high secondary flow rates at medium to high currents (48-180 A), exceeding the required values by nearly two-fold. However, it fails to provide any suction below 48 A. This represents an improvement over the work of Hosseinzadeh et al. [5], who could only achieve operation down to 60 A with their dual ejector design. Nevertheless, the challenge of designing a single ejector to cover the entire current range remains unresolved.

The integration of CFD and GA represents a scalable and efficient methodology for ejector optimization, offering significant cost and time savings while maintaining high accuracy. The findings provide a foundation for future research into advanced hydrogen recirculation technologies and their role in enhancing the efficiency and sustainability of clean energy systems. Future work will focus on further refining the optimization process, exploring additional operational parameters, and expanding the application of this framework to other fuel cell configurations. And moving from simulation to hardware, we will transition from computational models to empirical validation, developing a precision-engineered prototype to validate theoretical insights and demonstrate practical feasibility.

Declaration of Generative AI and AI-assisted technologies in the writing process

During the preparation of this work, the author(s) used Claude AI to enhance the clarity and readability of the textual description accompanying Figures 8 and 9. After using this tool, the author(s) reviewed and edited the content as needed and take(s) full responsibility for the content of the published article.

Acknowledgment

This research was supported by the EPSRC IAA (EP/X525856/1) (Engineering and Physical Sciences Research Council Impact Acceleration Award); conducted as part of the OptiSys project in collaboration with Rolls-Royce plc.

References

[1] Arabbeiki, M., Mansourkiaei, M., Ferrero, D., & Santarelli, M. (2024). Ejectors in Hydrogen Recirculation for PEMFC-Based Systems: A Comprehensive Review of Design, Operation, and Numerical Simulations. Energies, 17(19), 4815.

[2] Chen, L., Xu, K., Yang, Z., Yan, Z., Zhai, C., & Dong, Z. (2023). Optimal design of a novel nested-nozzle ejector for PEMFC's hydrogen supply and recirculation system. International Journal of Hydrogen Energy, 48(70), 27330-27343.

[3] Besagni, G., Mereu, R., Inzoli, F., & Chiesa, P. (2017). Application of an integrated lumped parameter-CFD approach to evaluate the ejector-driven anode recirculation in a PEM fuel cell system. applied thermal engineering, 121, 628-651.

[4] Yang, X., Long, X., & Yao, X. (2012). Numerical investigation on the mixing process in a steam ejector with different nozzle structures. International journal of thermal sciences, 56, 95-106.

[5] Hosseinzadeh, E., Rokni, M., Jabbari, M., & Mortensen, H. (2014). Numerical analysis of transport phenomena for designing of ejector in PEM forklift system. International journal of hydrogen energy, 39(12), 6664-6674.

[6] Jia, F., Yang, D., & Xie, J. (2021). Numerical investigation on the performance of two-throat nozzle ejectors with different mixing chamber structural parameters. Energies, 14(21), 6900.

[7] Banasiak, K., Hafner, A., & Andresen, T. (2012). Experimental and numerical investigation of the influence of the two-phase ejector geometry on the performance of the R744 heat pump. International journal of Refrigeration, 35(6), 1617-1625.

[8] Hakkaki-Fard, A., Aidoun, Z., & Ouzzane, M. (2015). A computational methodology for ejector design and performance maximisation. Energy Conversion and Management, 105, 1291-1302.

[9] Wang, L., Yan, J., Wang, C., & Li, X. (2017). Numerical study on optimization of ejector primary nozzle geometries. International Journal of Refrigeration, 76, 219-229.

[10] Chen, H., Zhu, J., Ge, J., Lu, W., & Zheng, L. (2020). A cylindrical mixing chamber ejector analysis model to predict the optimal nozzle exit position. Energy, 208, 118302.

[11] Nikiforow, K., Koski, P., Karimäki, H., Ihonen, J., & Alopaeus, V. (2016). Designing a hydrogen gas ejector for 5 kW stationary PEMFC system–CFD-modeling and experimental validation. International Journal of Hydrogen Energy, 41(33), 14952-14970.

[12] He, Y., Deng, J., Li, Y., & Zhang, X. (2021). Synergistic effect of geometric parameters on CO2 ejector based on local exergy destruction analysis. Applied Thermal Engineering, 184, 116256.

[13] Li, Y., & Deng, J. (2022). Numerical investigation on the performance of transcritical CO2 two-phase ejector with a novel non-equilibrium CFD model. Energy, 238, 121995.

[14] Liu, G., Wang, Z., Zhao, H., & Abdulwahid, A. H. A. (2022). R744 ejector simulation based on homogeneous equilibrium model and its application in trans-critical refrigeration system. Applied Thermal Engineering, 201, 117791.

[15] Liu, F., Li, Y., & Groll, E. A. (2012). Performance enhancement of CO2 air conditioner with a controllable ejector. International Journal of Refrigeration, 35(6), 1604-1616.

[16] Wu, Y., Zhao, H., Zhang, C., Wang, L., & Han, J. (2018). Optimization analysis of structure parameters of steam ejector based on CFD and orthogonal test. Energy, 151, 79-93.

[17] Le Tri, D. T., Vu, H. N., Woo, J., Kim, Y., & Yu, S. (2023). Optimization of the ejector parameters for anodic recirculation systems in high-performance dual-stack proton-exchange membrane fuel cells. Energy Conversion and Management, 296, 117712.

[18] Yan, J., Cai, W., & Li, Y. (2012). Geometry parameters effect for air-cooled ejector cooling systems with R134a refrigerant. Renewable energy, 46, 155-163.

[19] Kim, M., Lee, W. Y., & Kim, C. S. (2007). Development of the variable multi-ejector for a mini-bus PEMFC system. ECS Transactions, 5(1), 773.

[20] Brunner, D. A., Marcks, S., Bajpai, M., Prasad, A. K., & Advani, S. G. (2012). Design and characterization of an electronically controlled variable flow rate ejector for fuel cell applications. International journal of hydrogen energy, 37(5), 4457-4466.

[21] Pei, P., Ren, P., Li, Y., Wu, Z., Chen, D., Huang, S., & Jia, X. (2019). Numerical studies on wide-operating-range ejector based on anodic pressure drop characteristics in proton exchange membrane fuel cell system. Applied Energy, 235, 729-738.

[22] Kandakure, M. T., Gaikar, V. G., & Patwardhan, A. W. (2005). Hydrodynamic aspects of ejectors. Chemical Engineering Science, 60(22), 6391-6402.

[23] Zhu, Y., Cai, W., Wen, C., & Li, Y. (2009). Numerical investigation of geometry parameters for design of high performance ejectors. Applied Thermal Engineering, 29(5-6), 898-905.

[24] Bai, S., Wang, L., & Wang, X. (2017, October). Optimization of ejector geometric parameters with hybrid artificial fish swarm algorithm for PEM fuel cell. In 2017 Chinese Automation Congress (CAC) (pp. 3319-3322). IEEE.

[25] Shukla, P. B., Mydur, M., Nayak, S., & Krishna, V. (2021). Design optimization of ejectors using ANN and GA. In Proceedings of the 26thNational and 4th International ISHMT-ASTFE Heat and Mass Transfer Conference December 17-20, 2021, IIT Madras, Chennai-600036, Tamil Nadu, India. Begel House Inc.

[26] Chen, L., Xu, K., Yang, Z., Yan, Z., & Dong, Z. (2022). Optimal design and operation of dual-ejector PEMFC hydrogen supply and circulation system. Energies, 15(15), 5427.

[27] Liu, G., Pu, L., Zhao, H., Chen, Z., & Li, G. (2024). Multi-objective optimization of CO2 ejector by combined significant variables recognition, ANN surrogate model and multi-objective genetic algorithm. Energy, 295, 131010.

[28] Pang, Z., Han, J., Feng, J., Diao, A., Yao, Y., & Peng, X. (2024). Performance prediction and geometry optimization of ejector in PEMFC system using coupled CFD-BPNN and genetic algorithm. Applied Thermal Engineering, 123584.

[29] Maghsoodi, A., Afshari, E., & Ahmadikia, H. (2014). Optimization of geometric parameters for design a high-performance ejector in the proton exchange membrane fuel cell system using artificial neural network and genetic algorithm. Applied Thermal Engineering, 71(1), 410-418.

[30] Liu, G., Zhao, H., Deng, J., Wang, L., & Zhang, H. (2023). Performance improvement of CO2 two-phase ejector by combining CFD modeling, artificial neural network and genetic algorithm. International Journal of Refrigeration, 154, 151-167.

[31] Palacz, M., Smolka, J., Kus, W., Fic, A., Bulinski, Z., Nowak, A. J., ... & Hafner, A. (2016). CFD-based shape optimisation of a CO2 two-phase ejector mixing section. Applied Thermal Engineering, 95, 62-69.

[32] Palacz, M., Smolka, J., Nowak, A. J., Banasiak, K., & Hafner, A. (2017). Shape optimisation of a two-phase ejector for CO2 refrigeration systems. International journal of refrigeration, 74, 212-223.

[33] Carrillo, J. A. E., de La Flor, F. J. S., & Lissén, J. M. S. (2018). Single-phase ejector geometry optimisation by means of a multi-objective evolutionary algorithm and a surrogate CFD model. Energy, 164, 46-64.

[34] Ringstad, K. E., Banasiak, K., Ervik, Å., & Hafner, A. (2021). Machine learning and CFD for mapping and optimization of CO2 ejectors. Applied Thermal Engineering, 199, 117604.

[35] Li, Y., Deng, J., & He, Y. (2022). Numerical study on the interaction of geometric parameters of a transcritical CO2 two-phase ejector using response surface methodology and genetic algorithm. Applied Thermal Engineering, 214, 118799.

[36] Song, W., Shen, X., Huang, Y., Jiang, P., & Zhu, Y. (2023). Fuel ejector design and optimization for solid oxide fuel cells using response surface methodology and multi-objective genetic algorithm. Applied Thermal Engineering, 232, 121067.

[37] MV, S. R., & Jagadeesh, G. (2010). Vector evaluated particle swarm optimization (VEPSO) of supersonic ejector for hydrogen fuel cells.

[38] Gil, B., & Kasperski, J. (2018). Performance estimation of ejector cycles using ethers and fluorinated ethers as refrigerants. Applied Thermal Engineering, 133, 269-275.

[39] Rabbani, R. A., & Rokni, M. (2012). Dynamic simulation of a proton exchange membrane fuel cell system for automotive applications. In SEEP 2012 (pp. 311-316).

[40] Liso, V., Nielsen, M. P., Kær, S. K., & Mortensen, H. H. (2014). Thermal modeling and temperature control of a PEM fuel cell system for forklift applications. international journal of hydrogen energy, 39(16), 8410-8420.

[41] Hosseinzadeh, E., & Rokni, M. (2013). Development and validation of a simple analytical model of the proton exchange membrane fuel cell (PEMFC) in a fork-lift truck power system. International journal of green energy, 10(5), 523-543.

[42] Barbir, F. (2012). PEM fuel cells: theory and practice. Academic press.

[43] Lazar, A. L., Konradt, S. C., & Rotten Gruber, H. (2019). Open-source dynamic MATLAB/Simulink 1D proton exchange membrane fuel cell model. Energies, 12(18), 3478.

[44] Vahed, E., Khosravi, M., & Javan, M. (2024). Entrainment and mixing of unsteady gravity currents in compound channels. International Journal of Modern Physics C, 2450129, 27.

[45] Pétrowski, A., & Ben-Hamida, S. (2017). Evolutionary algorithms. John Wiley & Sons.

[46] Mitchell, M. (1998). An introduction to genetic algorithms. MIT press.

[47] Marsano, F., Magistri, L., & Massardo, A. F. (2004). Ejector performance influence on a solid oxide fuel cell anodic recirculation system. Journal of Power Sources, 129(2), 216-228.

Tables:

Table 1. Operating conditions for fuel cell stack recommended by manufacturer (Ballard).

Case	I [A]	A [cm^2]	P_{total} [W]	An_{Sto} [-]	Cat_{Sto} [-]	T_{ope} [K]	P_{an} [bar]	P_{cat} [bar]	Entrainment ratio [-]
T1	15	285.8	1414	6.3	5.1	334.15	1.15	1.08	16.34
T2	30	285.8	2723	3.4	2.4	336.15	1.16	1.10	8.09
T3	60	285.8	5201	2.2	1.8	339.15	1.31	1.17	4.25
T4	120	285.8	9794	1.9	1.8	340.15	1.57	1.35	2.83
T5	180	285.8	14157	1.6	1.8	340.65	1.92	1.58	1.72

Table 2. Design point values of ejector

Parameter	Marsano et al. [47]	Present study (CFD)
Primary flow composition (molar, %)	CH_4 (100)	CH_4 (100)
Secondary flow composition (molar, %)	H_2 (0.39); CO (4.19); H_2O; (43.96); CO_2 (51.46)	Average value of compositions
Primary mass flow rate (kg s-1)	0.0094	0.0092
Secondary mass flow rate (kg s-1)	0.0677	0.0676
Primary flow pressure (bar)	10.06	10.06
Secondary flow pressure (bar)	3.8	3.8
Outlet pressure (bar)	3.6	3.6
Primary flow Temperature (K)	673	673
Secondary flow Temperature (K)	1280	1280

Table 3. Predicted dimensions of the ejector using the genetic algorithm method.

Case	L_s [mm]	L_m [mm]	L_d [mm]	R_{th} [mm]	R_m [mm]	R_d [mm]	Suction [kg/s]	Entrainment ratio [-]
T3	0.28	16.0	45.45	0.23	1.5	5.09	0.0005133	7.45

List of Figures:

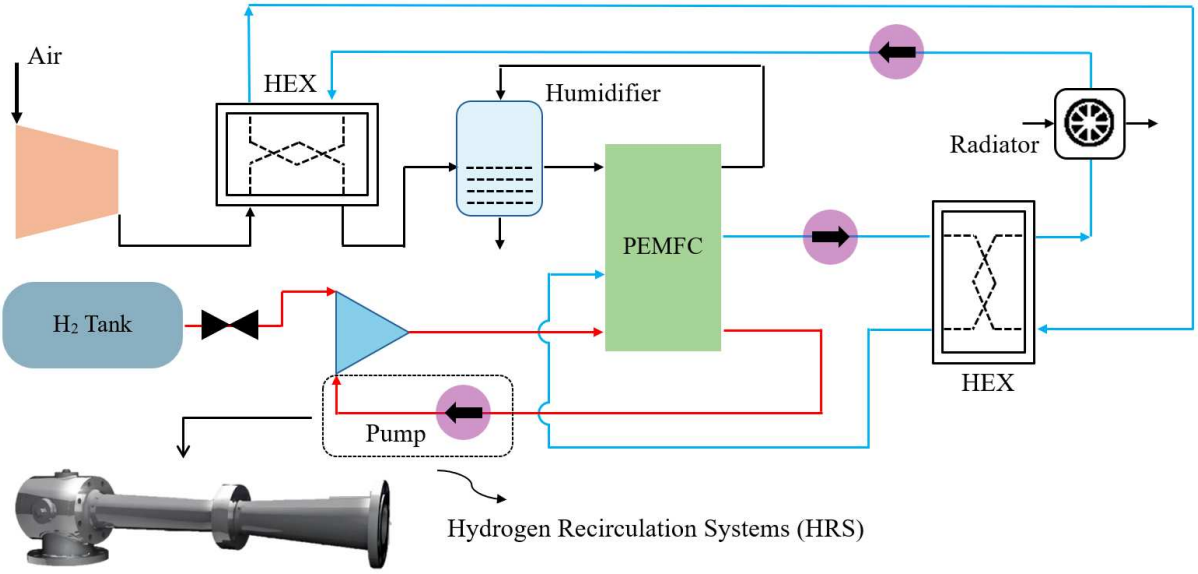

Figure 1. The schematic of the Ballard's fuel cell system configuration and its components (Air and hydrogen tank, Humidifier, Pump, Radiator, and Heat Exchanger).

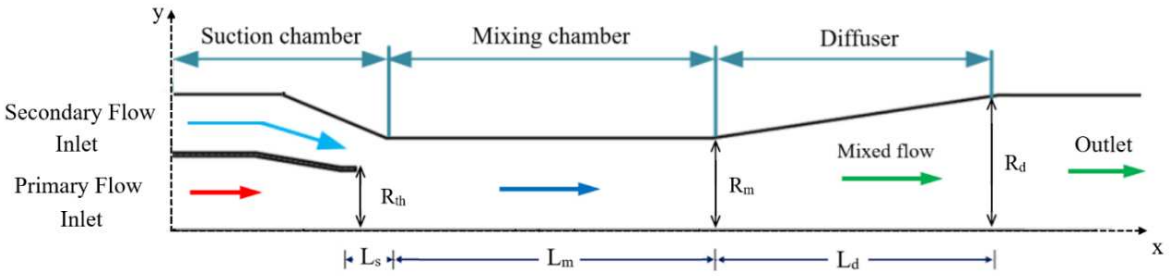

Figure 2. Schematic of the computational domain geometry, illustrating the arrangement and dimensions of the suction chamber, mixing chamber, and diffuser.

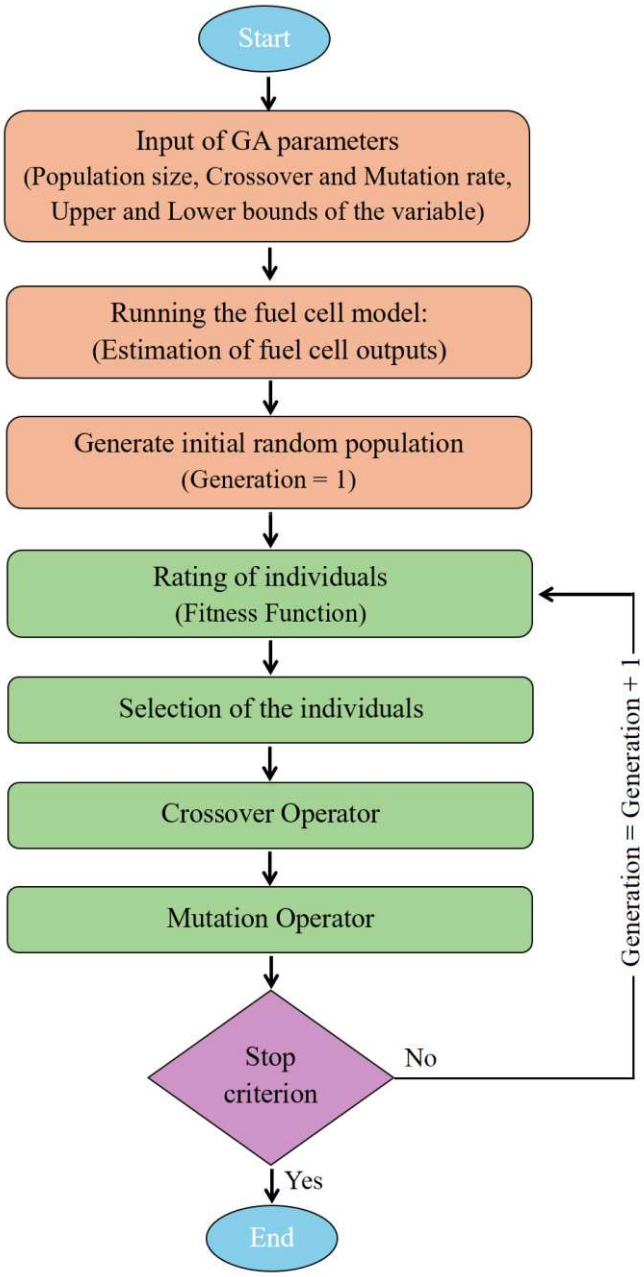

Figure 3. Genetic algorithm flowchart.

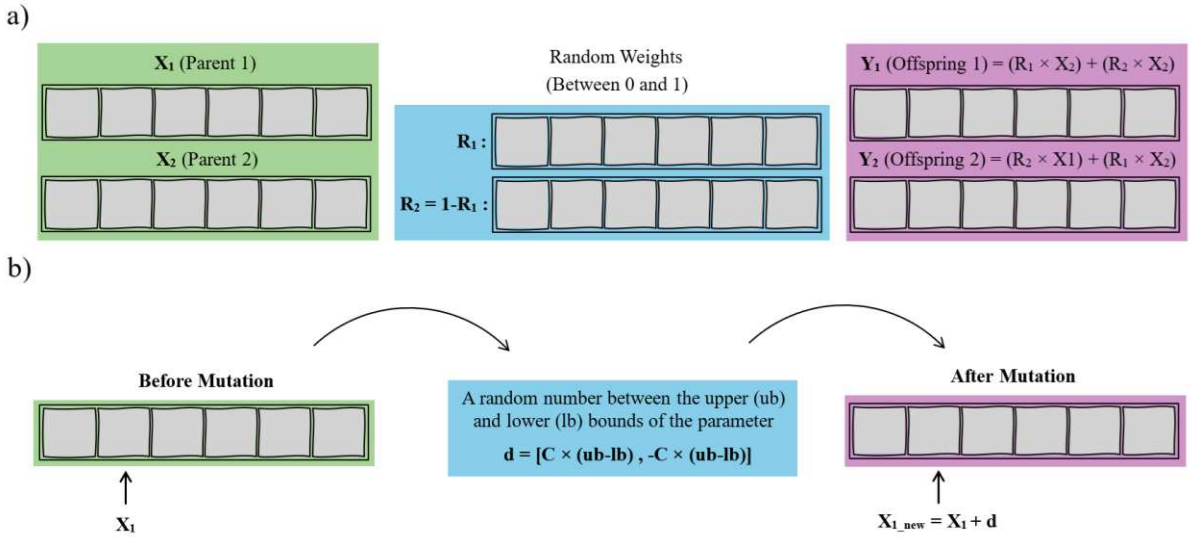

Figure 4. Operations of (a) continuous crossover and (b) continuous mutation from parent selection to offspring generation.

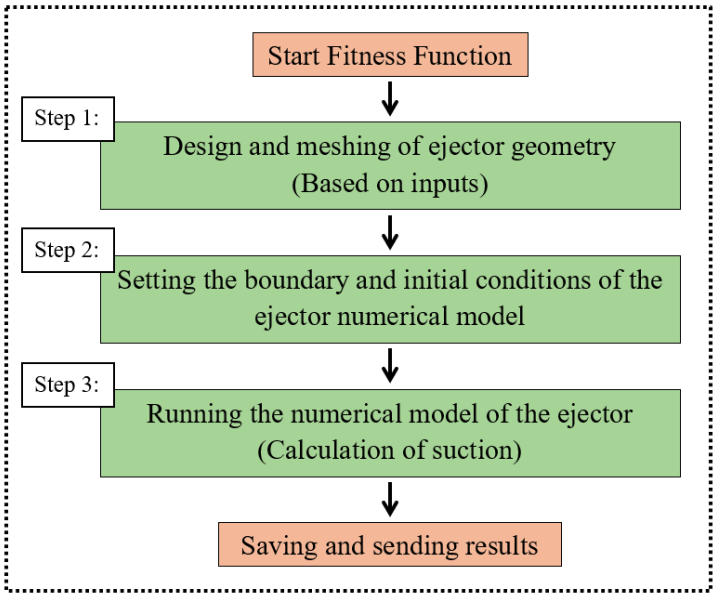

Figure 5. Flowchart of the fitness function for use in the genetic algorithm.

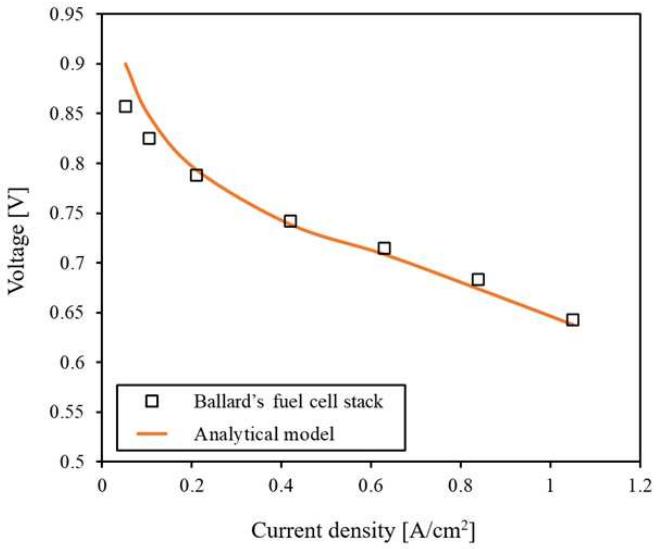

Figure 6. Comparison of polarization curves for different fuel cell temperatures. Symbols represent Ballard's fuel cell stack data, while the solid line depicts the analytical model results.

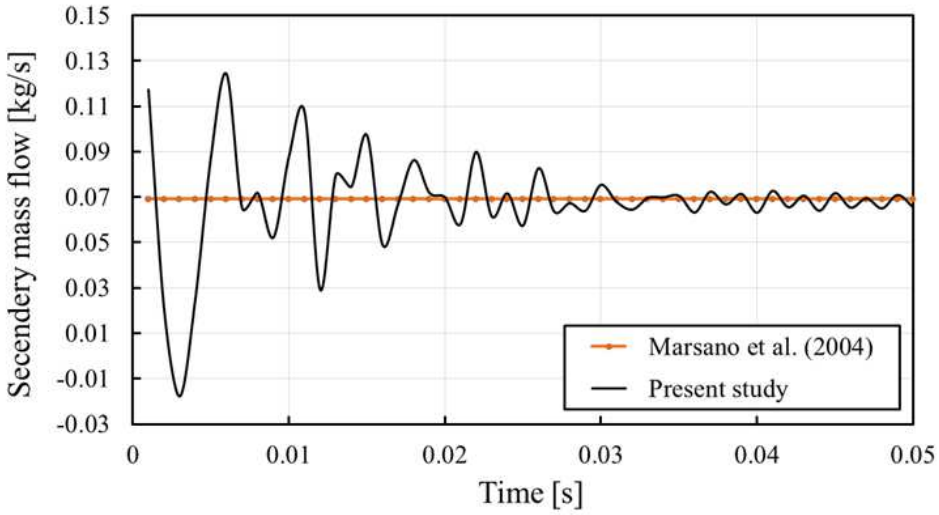

Figure 7. Comparison of Marsano et al. [47] data with results from the present numerical model for mass flow rate at the secondary flow inlet.

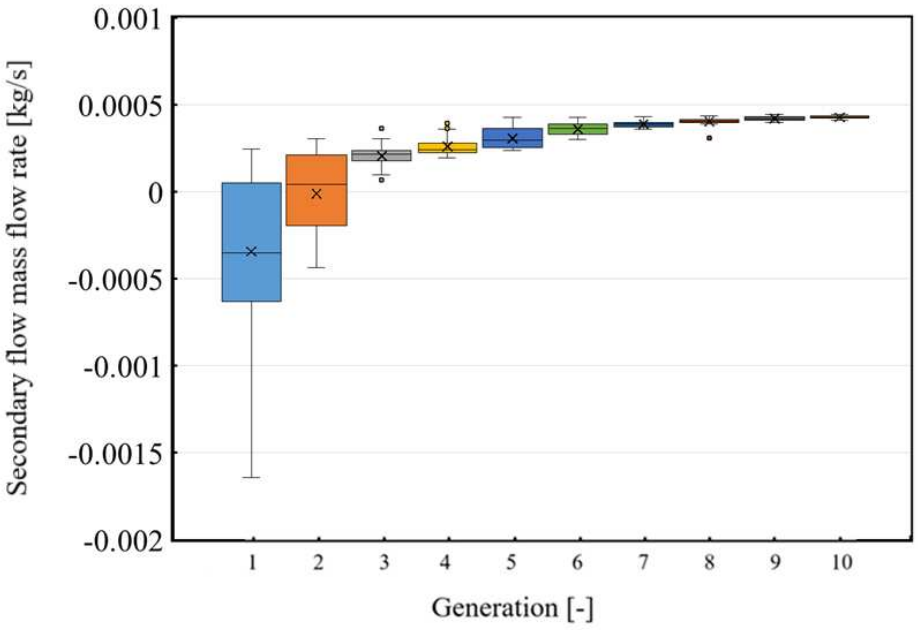

Figure 8. Box Plots displaying the distribution of data for each generation in case T3, illustrating the median, quartiles, and outliers within the dataset.

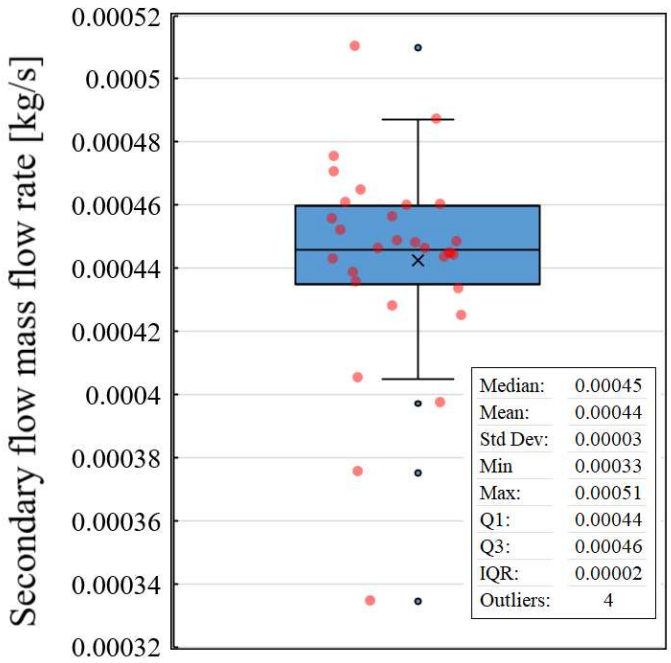

Figure 9. Box and whisker plot showing the results of 30 optimization runs for case T3.

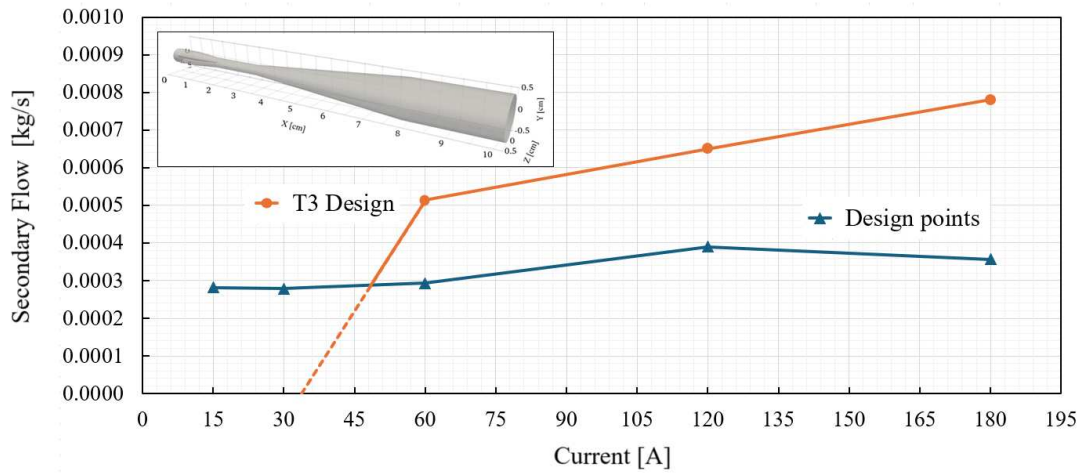

Figure 10. Profiles of the secondary flow rates extracted by the selected optimal ejector, accompanied by the corresponding design points.

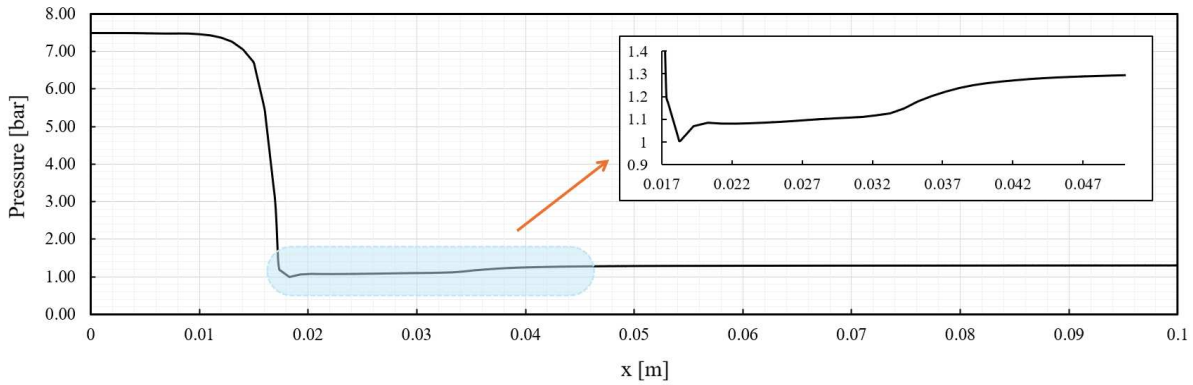

Figure 11. Pressure distribution profile along the x-axis of the ejector for I = 60 A, with a close-up view of the mixing chamber area.

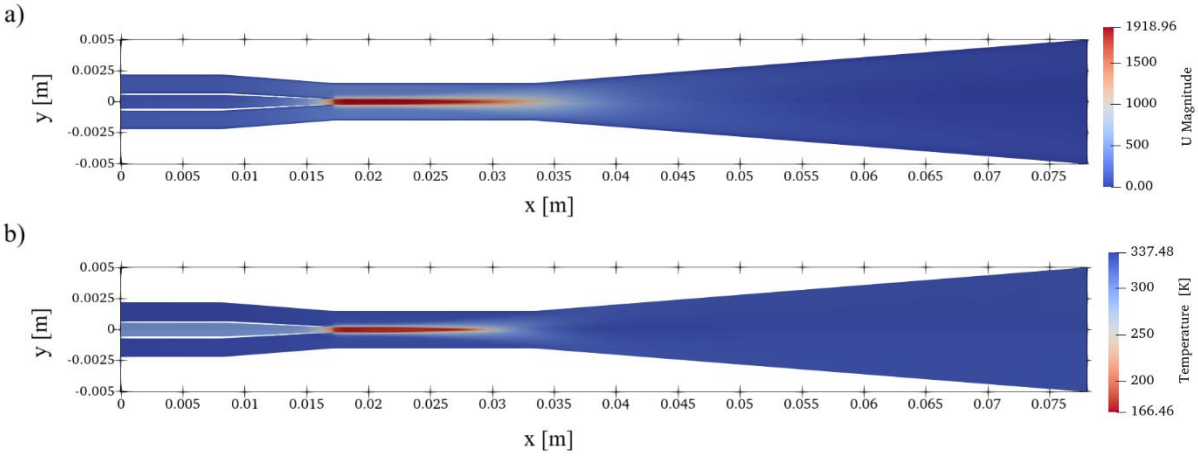

Figure 12. Contour plots of (a) velocity magnitude and (b) temperature distribution within the ejector at an operating current of 60 A.

Declaration of Interest Statement

☒ The authors declare that they have no known competing financial interests or personal relationships that could have appeared to influence the work reported in this paper.

☐ The author is an Editorial Board Member/Editor-in-Chief/Associate Editor/Guest Editor for this journal and was not involved in the editorial review or the decision to publish this article.

☐ The authors declare the following financial interests/personal relationships which may be considered as potential competing interests:

Elham Hosseinzadeh

https://orcid.org/0000-0002-5992-983X

Employment (1)

University of York: York, England, GB

2023-01 to present | Lecturer (School of Physics, Engineering and Technology)

Employment

Source: Elham Hosseinzadeh

Peer review (3)

- review activity for **Applied energy (5)**
- review activity for **Automotive innovation. (2)**
- review activity for **Journal of energy storage. (7)**

Record last modified Jul 15, 2025, 10:19:36 AM